

1 **Synchrotron FTIR and Raman spectroscopy provide unique spectral fingerprints for**
2 ***Arabidopsis* floral stem vascular tissues**

3

4 **Running title:** Spectral fingerprint of *Arabidopsis* vascular system

5

6 **Authors:** Dinant S¹, Wolff N¹, De Marco F¹, Vilaine F¹, Gissot L¹, Aubry E¹, Sandt C², Bellini
7 C^{1,3}, and Le Hir R^{1,*}

8

9 **Affiliations**

10 ¹ Institut Jean-Pierre Bourgin, INRA, AgroParisTech, CNRS, Université Paris-Saclay, 78000
11 Versailles, France

12 ² Synchrotron SOLEIL, Ligne SMIS, L'Orme des Merisiers, 91192 Gif sur Yvette, France

13 ³ Umeå Plant Science Centre, Department of Plant Physiology, Umeå University, 90183 Umeå,
14 Sweden

15

16 *: **Corresponding author:** Dr. R. Le Hir

17 Telephone: +33 1 30 83 30 57

18 Fax: +33 1 30 83 30 96

19 rozenn.le-hir@inra.fr

20 ORCID ID: 0000-0001-6076-5863

21

22 Co-authors email addresses:

23 Sylvie Dinant: sylvie.dinant@inra.fr

24 Nelly Wolff: nelly.wolff@inra.fr

25 Federica De Marco: demarco.federica@gmail.com

26 Françoise Vilaine: francoise.vilaine@inra.fr
27 Lionel Gissot: lionel.gissot@inra.fr
28 Emilie Aubry: emilia.aubry@inra.fr
29 Christophe Sandt: christophe.sandt@synchrotron-soleil.fr
30 Catherine Bellini: catherine.bellini@inra.fr, catherine.bellini@umu.se

31

32 Number of figures: 5

33 Number of tables: 6

34 Word count: 6113

35 Number of supplementary figures: 3

36

37 **Highlight (30 words)**

38 Combining vibrational spectroscopy techniques and multivariate analysis shows that the
39 disruption of *SWEET* genes impacts phloem cell wall composition and that the effect on xylem
40 cell wall composition is cell-specific.

41

42 **Abstract (200 words)**

43 Cell walls are highly complex structures that are modified during plant growth and
44 development. For example, the development of phloem and xylem vascular cells, which
45 participate in the transport of sugars and water as well as support, can be influenced by cell-
46 specific cell wall composition. Here, we used synchrotron radiation-based infrared (SR-FTIR)
47 and Raman spectroscopy to analyze the cell wall composition of wild-type and double mutant
48 *sweet11-1sweet12-1*, which impairs sugar transport, *Arabidopsis* floral stem vascular tissue.
49 The SR-FTIR spectra showed that in addition to modified xylem cell wall composition, phloem
50 cell walls in the double mutant line were characterized by modified hemicellulose composition.
51 Moreover, combining Raman spectroscopy with a Classification and Regression Tree (CART)
52 method identified combinations of Raman shifts that could distinguish xylem vessels and fibers.
53 Additionally, the disruption of *SWEET11* and *SWEET12* genes impacts xylem cell wall
54 composition in a cell-specific manner, with changes in hemicelluloses and cellulose observed
55 at the xylem vessel interface. These results suggest that the facilitated transport of sugars by

56 transporters that exist between vascular parenchyma cells and conducting cells is important to
57 ensuring correct phloem and xylem cell wall composition.

58

59 **Keywords (6-10 words)**

60 Arabidopsis, floral stem, phloem, xylem, cell wall, synchrotron radiation, FTIR, Raman
61 spectroscopy, multivariate analysis, CART method

62

63 **Introduction**

64 The presence of a polysaccharide-rich frame is an important feature of plant cells. The
65 primary cell wall, composed mainly of insoluble (cellulose and hemicelluloses) and soluble
66 polysaccharides (pectins), is deposited when plant cells are growing. Once the cells stop
67 growing, the primary cell wall is reinforced by a secondary cell wall (SCW), which is composed
68 mainly of cellulose, hemicelluloses and lignin. To ensure their specialized function in structural
69 support and water transportation, the xylem vessels and fibers have an even thicker SCW.
70 Secondary cell wall production in plant cells is of interest to humans because it constitutes the
71 major component of plant biomass and could therefore be used as a raw material for food,
72 clothing and energy. The model plant *Arabidopsis thaliana* can be used to study the SCW in
73 cells of vascular bundles within the floral stem (Strabala and MacMillan, 2013). Anatomically,
74 the vascular bundles are composed of phloem and xylem tissues and represent a central hub
75 through which most biological compounds are transmitted to their site of use. Phloem tissue -
76 composed of phloem parenchyma cells, companion cells and sieve elements (SE) - is involved
77 in the transport of multiple compounds such as sugars, amino acids, proteins and mRNA (Le
78 Hir *et al.*, 2008; Zhang and Turgeon, 2018). A thickening of the phloem SE cell wall has been
79 reported in *Arabidopsis*, and it was suggested that this cell wall is composed of pectic
80 polysaccharides (Freshour *et al.*, 1996). On the other hand, mature xylem tissue - responsible
81 for structural support as well as the transportation of water and solutes - is composed of xylem
82 tracheary elements (xylem vessels), xylary fibers and xylem parenchyma cells (Schuetz *et al.*,
83 2012), and is characterized by the presence of thick SCWs. Recently, researchers used high-
84 throughput immunolabelling of the major cell-wall glycan epitopes to cluster floral stem tissues
85 according to their cell wall composition, with the results revealing a tissue-specific pattern for
86 these glycan (Hall *et al.*, 2013). However, we still lack precise information about cell wall
87 composition at the cellular level. Among the tools that can provide spatial resolution at such a
88 level, vibrational microspectroscopy approaches boast several strong advantages.

89 Vibrational spectroscopy techniques (e.g. Fourier-transformed infrared spectroscopy
90 (FTIR), Raman spectroscopy) have been used extensively in plant research to decipher the cell
91 wall composition in an organ-specific manner (Largo-Gosens *et al.*, 2014). These
92 complementary techniques offer many advantages among which the spatial resolution, the non-
93 destruction of the samples and the cost-efficiency. They are also state-of-art techniques to study
94 the plant lignocellulosic biomass (i.e. biosynthesis, degradation and valorization) that is of
95 increasing interest due to its pivotal role for human and animal (i.e. food, energy, clothing,

96 building material) (Gierlinger, 2017). Classically, FTIR microspectroscopy uses a thermal
97 source to identify differences in the cell wall composition of wild-type and mutant of various
98 plant species with a spatial resolution of approximately 30-50 μm (Sibout *et al.*, 2005; Lefebvre
99 *et al.*, 2011; Le Hir *et al.*, 2015). The coupling of a focal plan array (FPA) detector to a
100 conventional FTIR microscope allows researchers to obtain structural information at the
101 cellular level (Gorzsás *et al.*, 2011; Ohman *et al.*, 2013). Another powerful modification is the
102 use of a synchrotron IR light source (SR-FTIR), which enables the collection of IR spectra at
103 higher spatial resolution (i.e. cellular level) due to light that is at least 100 times brighter than
104 that of a thermal source. However, this possibility has seen limited use in the plant biology field
105 (Vijayan *et al.*, 2015). In addition to IR microspectroscopy, Raman microspectroscopy is
106 commonly used to study plant cell wall composition (Gierlinger *et al.*, 2012; Gierlinger, 2017)
107 including that of xylem cell types (i.e. *Arabidopsis thaliana* (Prats Mateu *et al.*, 2016); *Cucumis*
108 *sativus* (Zeise *et al.*, 2018); *Malus* sp.: (Horbens *et al.*, 2014); *Populus* sp. (De Meester *et al.*,
109 2017; Jin *et al.*, 2018); *Picea* sp. (Agarwal, 2006; Hänninen *et al.*, 2011); *Pinus* sp. (Hänninen
110 *et al.*, 2011). To a lesser extent, the combined use of both techniques (e.g. FTIR and Raman
111 microspectroscopy) has been proven efficient and complementary in studying the xylem cell
112 wall composition in tree species such as Poplar (Özparpucu *et al.*, 2017, 2018) and *Pinus*
113 *radiata* (Zhang *et al.*, 2017).

114 Regarding the plant model *Arabidopsis thaliana*, only a few studies have investigated
115 the compositions of cell walls in the floral stem (Schmidt *et al.*, 2010; Prats Mateu *et al.*, 2016)
116 despite the important physiological role of this plant organ. The floral stem, which supports the
117 flowers and the fruits, is also a major contributor to lifetime carbon gain (Earley *et al.*, 2009),
118 representing 40% of a plant's total biomass. The precise characterization of the cell wall
119 compositions of different vascular cell types within the floral stem is necessary to better
120 understand cell wall complexity within such tissues.

121 In addition to the identification of differences in plant cell wall composition at the tissue
122 and cell levels, there are many unanswered questions regarding the modalities of sugar
123 allocation, which directly influence the supply of carbohydrate skeletons required for SCW
124 formation. We have previously focused on identifying the carbohydrate components underlying
125 xylem secondary cell wall formation in *Arabidopsis thaliana*. By using conventional FTIR
126 microspectroscopy, we identified cell wall modifications in the xylem of *Arabidopsis* double
127 mutant defective in the expression of sugar facilitators encoding genes *SWEET11* and
128 *SWEET12* (Le Hir *et al.*, 2015). Both genes encode proteins that transport sugars (sucrose,

129 glucose or fructose) along the concentration gradient (Chen *et al.*, 2012; Le Hir *et al.*, 2015)
130 and, as such, their disruption modifies cellulose and xylan acetylation in xylem cell walls within
131 the floral stem (Le Hir *et al.*, 2015). In that study, the FTIR spectra were acquired over a 30x30
132 μm target zone, which encompasses different cell types. Moreover, the use of conventional
133 FTIR on “dry-fixed” floral stem sections did not allow the acquisition of spectra describing
134 phloem tissue due to complete shrinkage of the tissue when the floral stem section is dry. As
135 *SWEET11* and *SWEET12* are expressed in both the phloem and xylem, spectral data at the
136 cellular level are needed to better understand how modifications of sugar homeostasis influence
137 the cell wall composition of various cell types (Chen *et al.*, 2012; Le Hir *et al.*, 2015).

138 In the presented work, we chose to use SR-FTIR and Raman microspectroscopy in
139 combination with a Classification and Regression Tree (CART) -based method to analyze
140 spectra collected for phloem and xylem tissues from *Arabidopsis thaliana* floral stem sections
141 of wild-type and *sweet11-1sweet12-1* double mutant plants (Fig. 1). Overall, we show that SR-
142 FTIR can be successfully used to analyze spectra acquired from phloem tissue, as well as that
143 changes in *SWEET11* and *SWEET12* expression affect phloem cell wall composition.
144 Additionally, the application of the CART method on Raman spectra shows that xylem vessels
145 and fibers can be distinguished by a combination of cellulose and hemicellulose Raman shifts.
146 Finally, our results suggest that facilitated sugar transport modifications in xylem parenchyma
147 cells lead to cell-specific defects.

148

149 **Materials and methods**

150 *Plant material and growth conditions*

151 *Arabidopsis* wild-type Col-0 line and *sweet11-1sweet12-1* (Le Hir *et al.*, 2015) double
152 mutants were grown in soil in a greenhouse for five weeks under long-day conditions (16 h
153 photoperiod and 150 $\mu\text{E m}^{-2} \text{ s}^{-1}$ light intensity) at 22/15°C (day/night temperature) with 65%
154 hygrometry. After five weeks of growth, the floral stem height is on average 25 cm for both
155 genotypes. The first five centimeters of the basal part of floral stem were collected, fixed in 4%
156 paraformaldehyde and embedded in paraffin. Sections with a thickness of 10 μm were deposited
157 onto BaF₂ windows and paraffin was removed using Histo-clear (National Diagnostics, Atlanta,
158 GA). For SR-FTIR and RAMAN spectroscopy, four xylem/phloem poles from four plants
159 representing each genotype were analyzed. Spectra were acquired on fully developed xylem
160 vessels and fibers localized in the middle of the vascular bundle.

161 *Synchrotron radiation FTIR microspectroscopy (SR-FTIR)*

162 Infrared spectra were recorded with a synchrotron source to provide better spatial
163 resolution due to superior brightness (SOLEIL, SMIS beamline, Gif sur Yvette, France). The
164 transmission spectra were collected on a NICOLET 5700 FT-IR spectrometer coupled to a
165 Continuum XL microscope (Thermo Fisher Scientific, Waltham, MA) equipped with a 32X
166 NA 0.65 objective as described in Guillon *et al.* (2011). All spectra were obtained in confocal
167 mode to eliminate diffraction from surrounding cells using a double path single masking
168 aperture size of 8 μm x 8 μm (Fig. S1B). The spectra were collected over the 1800-800 cm^{-1}
169 infrared range at a spectral resolution of 4 cm^{-1} with 256 co-added scans for the background
170 and sample spectra.

171

172 *Raman microspectroscopy*

173 The Raman spectra were recorded using a DXR Raman Instrument (Thermo Fisher
174 Scientific). Raman measurements were performed in a closed environment using a stabilized
175 532 nm laser as described in Zimmermann *et al.* (2015). A 100X NA 0.90 objective was used
176 for focusing and collecting inelastically scattered Raman light, and allowed us to reach a spatial
177 resolution of 2 μm x 2 μm (Fig. S1C). The acquisition points were set as the cell walls between
178 xylem vessels (VV), between xylem vessels and fibers (VF) and between xylem fibers (FF).
179 Overall the cell wall of 92 vessels and 126 fibers were analyzed in the WT floral stem while
180 the cell wall of 115 vessels and 123 fibers were analyzed in the double mutant line. The system
181 was operated in 25 μm aperture mode, which provided a spectral resolution of 2-4 cm^{-1} . In order
182 to decrease xylem cell wall autofluorescence, the samples were photobleached for two minutes
183 before each acquisition. Sample spectra were acquired over an exposure time of 6 x 10 s using
184 512 scans (the same amount of scans were also performed for the background).

185

186 *Preprocessing of SR-FTIR and Raman spectra*

187 Infrared spectra with extreme absorbance values, e.g. values less than 0.1 or above 1,
188 were removed from the datasets so that saturation effects and errors due to holes in the tissue
189 sections could be avoided. Spectra comparison between tissue or genotype was performed on
190 baseline-corrected and area-normalized spectra. For Raman microspectroscopy, the spectra of
191 different xylem cell types were smoothed by the Savitsky-Golay algorithm (3rd order
192 polynomial and nine-point filter). The spectra were then baseline-corrected by subtracting a

193 linear baseline between 350-3500 cm⁻¹ and area-normalized. Both SR-FTIR and Raman spectra
194 were preprocessed using Unscrambler software (The Unscrambler, CAMO Process AS, Oslo,
195 Norway).

196

197 *Univariate analysis of the SR-FTIR and Raman spectra*

198 Peak area measurements were performed on baseline-corrected and area-normalized
199 FTIR spectra in OMNIC 9.2.41 and TQ Analyst EZ 9.2.34 software (Thermo Scientific). In
200 both cases, the baseline between the peak start and end marker was computer generated. The
201 following peaks were measured for the SR-FTIR spectra: 930-1180 cm⁻¹ for cellulose; 1695-
202 1770 cm⁻¹ for hemicellulose; and 1475-1520 cm⁻¹ for lignin. Average spectra and boxplot
203 representations were generated in R software (R Development Core Team, 2016) using the
204 HyperSpec and Ggplot2 packages, respectively (Wickham, 2009; Beleites, 2012). Peak areas
205 and their ratios were first checked for normality (Shapiro-Wilk test) and homoscedasticity
206 (Levene test). Since neither of these criteria were fulfilled, an approximate (Monte Carlo)
207 Fisher-Pitman permutation test was performed (non-parametric one-way ANOVA). Then, a
208 pairwise comparison test, including the calculation of an adjusted *P*-value by the False
209 Discovery Rate (FDR) method, was applied to assess the significance of observed differences.
210 Statistical analysis was performed using the “coin”, and “RVAideMemoire” packages (Hothorn
211 *et al.*, 2008; Maxime, 2017) in R software (R Development Core Team, 2016).

212

213 *Multivariate statistical analysis of SR-FTIR and Raman spectra*

214 Preprocessed and mean-centered spectra were first subjected to Principal Component
215 Analysis (PCA). The PCA was carried out with three to seven principal components (PC) using
216 the NIPALS algorithm, and full cross-validation was applied. Outliers identified using the
217 Hotelling T2 method (95% multivariate confidence interval) and the residual versus leverage
218 plot were removed from the dataset. Since SR-FTIR and Raman techniques produce large
219 dataset and variables are highly correlated, a variable selection algorithm (CovSel) was applied
220 prior to the Classification and regression tree (CART) technique. The CovSel algorithm enables
221 variable selection based on global covariance across all the responses (Roger *et al.*, 2011).
222 Additionally, the CART technique can be used to select the variables that are most important
223 to discriminating two factors (Berk, 2016). The CART-based model was first set up on a

224 calibration dataset (representing 80% of the total spectra) and then validated on a validation
225 dataset (representing 20% of the total spectra). A confusion table was then produced to validate
226 the model. Model performance was evaluated using the following parameters: accuracy
227 $(\frac{\Sigma \text{true positive} + \Sigma \text{true negative}}{\Sigma \text{total population}})$; specificity $(\frac{\Sigma \text{true positive}}{\Sigma \text{true positive} + \Sigma \text{false negative}})$; sensitivity
228 $(\frac{\Sigma \text{true negative}}{\Sigma \text{true negative} + \Sigma \text{false positive}})$; predictive positive value $(\frac{\Sigma \text{true positive}}{\Sigma \text{true positive} + \Sigma \text{false positive}})$; and
229 negative predictive value $(\frac{\Sigma \text{true negative}}{\Sigma \text{true negative} + \Sigma \text{false negative}})$. In the comparison of both genotypes,
230 the true positive and true negative represent the number of wild-type or *sweet11-1sweet12-1*
231 spectra that were correctly classified by the model. The false positive and false negative
232 represent the number of wild-type or *sweet11-1sweet12-1* spectra that were incorrectly
233 classified by the model. The multivariate analyses were performed in the ChemFlow interface
234 within Galaxy (<https://vm-chemflow.toulouse.inra.fr/>).

235

236 **Results and discussion**

237 *Synchrotron radiation FTIR (SR-FTIR) allows the identification of unique spectral fingerprints*
238 *for the floral stem vascular tissues.*

239 In the *Arabidopsis* floral stem, vascular tissues are organized as a series of vascular
240 bundles that are connected together by the interfascicular cambium (Fig. S1A). In each bundle,
241 specialized conducting cells are subjected to high pressures to ensure sap flow, with hydrostatic
242 pressure reaching upwards of 30 atmospheres in the sieve elements (Sjölund, 1997) while the
243 xylem vessels are characterized by negative pressure. Cell-specific cell wall composition is a
244 crucial part of conferring resistance to such pressure. A majority of the previous research has
245 focused on deciphering xylem cell wall composition, while phloem tissue has received limited
246 attention.

247 By harnessing the spatial resolution provided by Synchrotron light (8x8 μm acquisition
248 zone), we acquired spectra for phloem and xylem tissues of the *Arabidopsis* wild-type floral
249 stem (Fig. 1 and Fig. S1A). Spectra were baseline corrected, area-normalized and the average
250 spectrum for each tissue was calculated and plotted (Fig. 2A). Principal component analysis
251 (PCA) was used to identify potential spectral fingerprints of the floral stem vascular tissues,
252 with the first two components explaining 54% and 8% of the total variance (Fig. 2B).
253 Component 1 undoubtedly discriminates the phloem and xylem IR spectra (Fig. 2B). The
254 loading plot of PC1 reveals that xylem cell walls are characterized by a set of bands
255 corresponding to guaiacyl ring breathing with carbonyl stretching (1269 cm^{-1}) (Kubo and
256 Kadla, 2005), -C-H- deformation in the guaiacyl ring with -C-O- deformation in the primary
257 alcohol (1030 cm^{-1}) (Kubo and Kadla, 2005) and -C-C- linkage of G-condensed units (1060 cm^{-1}).
258 This suggests that xylem cell walls are mainly composed of G-type lignin (Fig. 2C and
259 Table 1), and these results are in agreement with previous observations from *Arabidopsis*
260 *thaliana* that showed that G-type lignin is responsible for the extra-thickening of the xylem
261 vessel cell wall (Schuetz *et al.*, 2012). Additionally, the loading plot highlights several
262 wavenumbers ($1045, 1369, 1230-1235, 1743, 1245, 1735-1740\text{ cm}^{-1}$) that are related to
263 hemicellulose enrichment in xylem cell walls, as has been previously reported for the
264 *Arabidopsis* floral stem (Table 1) (Sibout *et al.*, 2005; Ohman *et al.*, 2013). However, some of
265 these bands may partly overlap with the lignin bands ($1236, 1371$ and 1736 cm^{-1}) (Faix, 1991;
266 Özparpucu *et al.*, 2018).

267 Interestingly, wavenumbers associated with pectic polysaccharides (1245 and 1762 cm⁻¹)
268 were also found to be more descriptive of xylem cell walls than of phloem cell walls (Fig.
269 2C and Table 1), even if pectins are not an abundant component of secondary cell walls.
270 However, pectin methylesterification appears to be a prerequisite for the lignin modification
271 that occurs during secondary cell wall deposition in xylem cells (Pelloux *et al.*, 2007). In
272 addition, several *Arabidopsis* mutants that are deficient in various pectins have been shown to
273 present defects in secondary cell wall formation (Persson *et al.*, 2007; Lefebvre *et al.*, 2011).

274 Regarding phloem cell wall composition, the loading plot of PC1 reveals numerous
275 wavenumbers related to pectic polysaccharides, cellulose and hemicelluloses (Fig. 2C and
276 Table 1). For instance, the bands at 1639 cm⁻¹ and at 1677 cm⁻¹ are characteristic of the -COOH-
277 group of acidic pectins present in the primary cell wall (Mouille *et al.*, 2006), while
278 wavenumbers at 1111, 1157 and 1550 cm⁻¹ describe cellulose polymers (Table 1). Additionally,
279 wavenumbers at 1442 and 1475 cm⁻¹ were unique for phloem cell walls. The 1442 cm⁻¹ band
280 has been previously reported to describe the hypocotyl primary cell wall of a cellulose-deficient
281 mutant, but the functional group that it represents still needs to be verified (Mouille *et al.*, 2003).
282 Overall, these results suggest that the cell wall composition of phloem tissue, including phloem
283 parenchyma cells, companion cells and sieve elements, is more closely related to primary cell
284 wall composition even if cell wall thickening is commonly observed in sieve elements (SEs)
285 (Esau and Cheadle, 1958). The nature of this thickening has not yet been completely clarified,
286 but the current evidence favors a pectin-based composition (Freshour *et al.*, 1996; Torode *et*
287 *al.*, 2018). The marker IR bands we identified in our tissue samples support these findings. It
288 was initially surprising that pectins, which have been traditionally related to cellular expansion,
289 can be found in a tissue that experiences high pressure during sap flow. The recent
290 characterization of an antibody against branched pectic galactan that specifically binds to the
291 cell walls of SEs led the authors to suggest that the role of pectin in these cell walls could be
292 the maintenance of elastic properties required for withstanding high turgor pressure (Torode *et*
293 *al.*, 2018). Additionally, the application of atomic force microscopy (AFM) has shown that the
294 mechanical properties of phloem SE cell walls differ from those of cells from the surrounding
295 tissue with an higher elasticity (Johnson, 2018; Torode *et al.*, 2018). The recent development
296 of the nano-IR techniques that combine AFM and Synchrotron IR light (Pereira *et al.*, 2018)
297 will open further possibilities for exploring the cell wall heterogeneity that exists among
298 different vascular cell types. Further the implementation of microfluidic infrared spectroscopy
299 to study plant sample in a liquid environment represents an important progress (Devaux *et al.*,

300 2018) especially to study plant tissue that are not accessible anymore after the dehydration
301 process, usually required for IR analysis, such as the phloem tissue.

302 *Phloem cell wall composition is impaired in the double mutant sweet11-1sweet12-1.*

303 In addition to presence in the xylem tissue, *SWEET11* and *SWEET12* expression has
304 also been detected in phloem tissue, with the signal arising from phloem parenchyma cells
305 (Chen *et al.*, 2012; Le Hir *et al.*, 2015). Since the double mutant *sweet11-1sweet12-1* shows
306 defects in xylem cell wall formation, we analyzed whether similar defects in cell wall formation
307 could be observed in phloem cells. Therefore, phloem and xylem IR spectra were recorded from
308 the double mutant *sweet11-1sweet12-1* floral stem and compared to spectra acquired from the
309 wild-type floral stem (Fig. 1). The average spectra for wild-type (WT) and double mutant (DM)
310 tissues were compared after baseline correction and area normalization over the 1800-850 cm⁻¹
311 range (Supplementary Fig S2A and S2E). Next, the areas under the cellulose (C-O and C-C
312 stretching) (930-1180 cm⁻¹), the hemicellulose (1695-1770 cm⁻¹) and/or lignin (1475-1520 cm⁻¹)
313 peaks, along with their respective ratios, were measured (Fig. 3 and Supplementary Fig. S2B-
314 D and S2F-G). A significant decrease in the lignin peak area of the xylem tissue was measured
315 between both genotypes (Supplementary Fig. S2D), while a significant increase in the cellulose
316 and the hemicelluloses peak areas was observed in xylem cell walls in the double mutant line
317 compared to the wild-type (Supplementary Fig. S2B and C). The phloem tissue analysis showed
318 that there was no significant difference in cellulose between the two genotypes (Supplementary
319 Fig. S2F), while the hemicelluloses peak area in the double mutant line was significantly greater
320 than what was observed in the wild-type (Supplementary Fig. S2G). More precisely, while the
321 xylem cell walls of both genotypes showed similar cellulose/hemicellulose ratios (Fig. 3A), the
322 phloem cell walls of the double mutant demonstrated a disequilibrium in the
323 cellulose/hemicellulose ratio (Fig. 3B). Therefore, we show that in addition to affecting xylem
324 cell wall composition, mutations in both *SWEET11* and *SWEET12* genes also impact phloem
325 cell wall composition. However, these mutations seem to only affect the hemicellulose
326 composition of phloem cell walls.

327 In order to further identify wavenumbers that could be specifically associated with the
328 *sweet11-1sweet12-1* double mutant, we applied a CART analysis procedure. For this purpose,
329 our original dataset was split into calibration (80% of the total dataset) and validation (20% of
330 the total dataset) datasets, after which the CovSel algorithm was applied to the calibration
331 dataset to identify the 10 wavenumbers with maximum covariance (Roger *et al.*, 2011). The
332 CART tree resulting from the analysis shows that, out of the 10 selected wavenumbers, only

333 five IR wavenumbers - at 891, 1086, 1369, 1562 and 1712 cm^{-1} – can be used to distinguish
334 between the wild-type and *sweet11-1sweet12-1* phloem spectra (Fig. 3C). To evaluate the
335 performance of this analysis, the CART model obtained from the calibration dataset was used
336 as an input and applied on the validation dataset. Table 2 summarizes the results of both
337 genotypes for the model calibration (after ten-fold cross-validation) and validation datasets.
338 When applied on the calibration dataset, the CART model correctly classified 88.6% of the
339 wild-type spectra (specificity) and 92.5% (sensitivity) of the double mutant spectra. When
340 applied on the validation dataset, the model correctly classified 82.7% (specificity) and 79.5%
341 (sensitivity) of the WT and DM spectra, respectively. Moreover, the predictive positive value
342 (PPV) of the validation model was calculated to be 75%, which means that most of the
343 identified WT spectra are not false positives (Table 2). On the other hand, the model's negative
344 predictive value (NPV) was determined to be 86.1%, which means that a majority of the
345 identified *sweet11-sweet12-1* DM spectra are not false positives (Table 2). Overall, the CART
346 model was able to accurately predict 80.8% of the spectra present in the validation dataset
347 (Table 2). In this way, the CART model produced using the calibration dataset can discriminate
348 both genotypes based only on the analysis of five major FTIR wavenumbers. Among these
349 marker wavenumbers, the 891 cm^{-1} wavenumber can be linked to the cellulose fingerprint
350 region (Kačuráková *et al.*, 2002) while the 1086 cm^{-1} and 1369 cm^{-1} wavenumbers can be
351 assigned to hemicelluloses (Robin *et al.*, 2003; Brown *et al.*, 2005). Additionally, the 1712 cm^{-1}
352 wavenumber could be related to carboxylic acid residues found in polygalacturonic acid
353 (Pawar *et al.*, 2013). The remaining wavenumber, 1562 cm^{-1} , still needs to be assigned to a cell
354 wall compound. Interestingly, we previously found that the 1369 cm^{-1} wavenumber (this work
355 and (Le Hir *et al.*, 2015)) can differentiate WT xylem cell walls from the cell walls of the
356 *sweet11-sweet12-1* double mutant. This wavenumber is related to the deformation of C–H
357 linkages in the methyl group of *O*-acetyl moieties and could thus represent differences in xylan
358 acetylation (Mohebby, 2010). Therefore, the presented results suggest that sugar homeostasis
359 modifications in plant vascular tissue predominantly influence the cellulose and/or xylan
360 composition of cell walls regardless of cell type.

361 We previously postulated that the maintenance of sugar homeostasis among the xylem
362 parenchyma cells and xylem vessels/fibers influenced the production of a normal cell wall (Le
363 Hir *et al.*, 2015). Here, we show that it also constitutes a limiting step for the formation of
364 phloem cell walls. Since *SWEET11* and *SWEET12* are expressed in the phloem and xylem
365 parenchyma cells and participate in sugar influx or efflux across the plasma membrane (Chen
366 *et al.*, 2012; Le Hir *et al.*, 2015), our data suggest that *SWEET11* and *SWEET12* are crucial for

367 cell wall formation in vascular parenchyma cells. Interestingly, recent research has also found
368 vascular parenchyma cells to be crucial in the supply of monolignols to developing xylem
369 vessels (Smith *et al.*, 2017). Therefore, one could postulate that sugar (sucrose and/or hexoses)
370 movement across a gradient, mediated by SWEET11 and/or SWEET12, could also occur
371 between vascular parenchyma cells and other developing vascular cells to drive cell wall
372 formation.

373

374 *Identification of new Raman shift markers that describe the composition of cell walls between*
375 *different xylem cell types in the wild-type Arabidopsis floral stem*

376 Xylem secondary cell wall formation constitutes a large pool of the plant's total
377 biomass. For example, the xylem vessels and fibers are surrounded by a thick SCW that is 80%
378 cellulose and hemicelluloses and 20% lignin (Marriott *et al.*, 2016). When the Arabidopsis
379 floral stem is considered at the cellular level, xylem vessels and fibers demonstrate
380 heterogeneous cell wall composition due to differences in the lignin monomer(s) with which
381 the cell wall is enriched (Schuetz *et al.*, 2012). Unfortunately, we still lack a complete
382 description of the polysaccharide composition of xylem vessel and fiber cell walls. We
383 leveraged the spatial resolution provided by Raman microspectroscopy to precisely characterize
384 the composition of cell walls between xylem vessels (VV), between xylem vessels and xylem
385 fibers (VF) and between xylem fibers (FF) in the Arabidopsis wild-type floral stem (Fig. 1, Fig.
386 S1C, Fig. 4 and Supplementary Fig. 3).

387 The average Raman spectra for the various xylem cell types show that xylem fiber cell
388 wall composition differs in comparison to what was observed in the other two cell types
389 (Supplementary Fig. S3A). To test whether these differences were statistically significant, we
390 calculated ratios of spectral peaks areas from already known Raman shift markers, namely,
391 from 2775 to 3125 cm^{-1} (the composite C-H stretching bands comprising cellulose and
392 hemicelluloses), from 1550 to 1700 cm^{-1} (lignin Raman shift) and from 1080 to 1140 cm^{-1} (C-
393 O and C-C bond stretches of cellulose) (Schmidt *et al.*, 2010; Agarwal, 2014) (Fig. 4). Based
394 on these measurements, the VV and VF cell walls in wild-type Arabidopsis plants could not be
395 statistically distinguished (Fig. 4A-C). However, the ratio of lignin to C-H bonds as well as the
396 ratio of lignin to C-O bonds can significantly discriminate the cell walls between xylem fibers
397 (FF) from those between xylem vessels (VV) and xylem vessels and fibers (VF) (Fig. 4A and
398 4B). There were no significant differences in the ratio of C-H bonds to C-O bonds between cell
399 types (Fig. 4C). Therefore, the observed differences between cell walls between VV, VF and

400 FF can mainly be attributed to a lower intensity of the aromatic ring stretching vibration
401 (1598 cm^{-1}) in the cell walls between xylem fibers (Fig. S3A) (Özparpucu *et al.*, 2017).

402 To further identify Raman shifts associated with different xylem cell types, a CART-
403 based classification method was applied on the $1000\text{-}1800\text{ cm}^{-1}$ Raman shift range, which
404 includes the predominant constituents of the xylem cell wall (Prats Mateu *et al.*, 2016;
405 Özparpucu *et al.*, 2017). The CART model was built on the calibration dataset (80% of the total
406 dataset), without a variable selection step, and the resulting classification tree shows that only
407 four Raman shifts are sufficient to distinguish the three different cell wall types (Fig. 4D). The
408 overall accuracy of the model produced from the calibration dataset was 85.9%, with good
409 prediction values (PPV) of 100%, 77.7% and 83.3% for the VV, VF and FF groups, respectively
410 (Table 3). This model was then applied to the validation dataset (20% of the total dataset), and
411 showed an accuracy value of 80%, which is close to that of the calibration dataset (Table 3).
412 Even though the predictive sensitivity for spectra between adjacent xylem vessels (VV) was
413 low, with only 50% of spectra correctly classified as VV spectra (Table 3), the PPVs for VF
414 and FF spectra (87.5 and 100%, respectively) were good (Table 3). Therefore, our CART model
415 can be used to distinguish VF and FF spectra, but the results should be interpreted with caution
416 in the case of VV spectra. Nevertheless, our data show that the $1038, 1118, 1408$ and 1258 cm^{-1}
417 Raman shifts can be used to discriminate most of the different xylem cell wall types in wild-
418 type *Arabidopsis* plants. Interestingly, the band around 1038 cm^{-1} was reported to describe C-
419 O stretching of mannan oligosaccharides (Maru *et al.*, 2015) while the Raman shift around 1256 cm^{-1}
420 has been linked to hemicelluloses (Gierlinger *et al.*, 2008). The bands at 1121 cm^{-1}
421 (symmetric $\nu(\text{COC})$ glycosidic bond) and 1408 cm^{-1} ($\delta(\text{CH}_2)$ region) have also been assigned
422 to cellulose (Edwards *et al.*, 1997; Chylinska *et al.*, 2014).

423 Earlier studies in *Arabidopsis* have clearly established that the cell walls of xylem
424 interfascicular fibers and xylem vessels differ in terms of their lignin monomer composition
425 (Schuetz *et al.*, 2012). Additionally, results from Poplar studies suggest that the cell wall
426 composition of xylem fibers is an intermediate between that of xylem interfascicular fibers and
427 xylem vessels (Gorzsás *et al.*, 2011). ToF-SIMS has previously been applied to measure
428 differences in the S/G ratio between xylem fibers and vessels in *Populus* (Tolbert *et al.*, 2016).
429 Our work shows that a combination of Raman shifts assigned to cellulose and hemicelluloses
430 can also distinguish xylem cell types. This is in agreement with previous research, as the
431 immunolabelling of mannan epitopes (LM10 and LM11 antibodies) in the *Arabidopsis* floral
432 stem revealed a higher signal intensity in xylem fibers than in xylem vessels (Kim and Daniel,

433 2012). This higher intensity of mannans in the xylem fiber cell wall could suggest that these
434 compounds are more important to mechanical support than water conduction (Kim and Daniel,
435 2012).

436

437 *Disruption of SWEET11 and SWEET12 expression differentially affects the cell wall*
438 *composition of different xylem cell types*

439 To further understand how modifications in facilitated sugar transport influence xylem
440 secondary cell wall formation, we acquired Raman spectra for different xylem cell types from
441 the *sweet11-1sweet12-1* double mutant (Fig. 1). As previously described, CART-based
442 classifications were built to compare the different xylem cell types from both genotypes. For
443 each cell type (VV, VF or FF), the original dataset was split into a calibration dataset and a
444 validation dataset, after which the CovSel algorithm was applied on the calibration dataset to
445 select the 10 Raman shifts showing maximum covariance. The CART models were then built
446 on the calibration datasets and later applied on the validation datasets (Table 4, 5 and 6). The
447 resulting CART tree classifications are displayed in Fig. 5. Regarding the cell walls between
448 adjacent xylem vessels, two Raman shifts, namely, 1001 and 1093 cm^{-1} , were sufficient to
449 differentiate wild-type spectra from the double mutant spectra (Fig. 5A). Interestingly, these
450 two Raman shifts have been shown to be associated with cellulose compounds (Gierlinger and
451 Schwanninger, 2007; Özparpucu *et al.*, 2017). Model performance was estimated for both
452 calibration and validation datasets (Table 4), with the results demonstrating that the model can
453 accurately discriminate spectra from both genotypes since the overall accuracy, sensitivity,
454 specificity, PPV and NPV calculated for the validation dataset were between 76% and 90 %
455 (Table 4).

456 Additionally, data obtained from the CART model produced using Raman spectra
457 acquired for the walls between xylem vessels and fibers (VF spectra) show that seven Raman
458 shifts - at 1093, 1134, 1296, 1372, 1606, 1618 and 1743 cm^{-1} – can be used to discriminate the
459 genotypes (Fig. 5B). The 1093 cm^{-1} shift appears three times and the 1296 and 1743 cm^{-1} shifts
460 appear twice in the CART tree, suggesting that these three shifts are most important to
461 discriminating the two genotypes (Fig. 5B). Based on the literature, the 1093 and 1372 cm^{-1}
462 shifts are related to cellulose (Chylinska *et al.*, 2014; Özparpucu *et al.*, 2017), while the 1743
463 cm^{-1} is assigned to the $\nu(\text{C}=\text{O})$ ester in pectins or hemicelluloses compounds (Chylinska *et al.*,
464 2014). The 1606 and 1618 cm^{-1} Raman shifts have been reported to describe lignin bands (Prats

465 Mateu *et al.*, 2016). The performance of the model produced from VF spectra (for both
466 calibration and validation datasets) was similar to the previous model.

467 Finally, the CART tree built using the spectra acquired for the walls between adjacent
468 xylem fibers (FF spectra) shows that four Raman shifts can be used to discriminate between the
469 wild-type and double mutant spectra. These shifts occur at 1134, 1332, 1597 and 1691 cm⁻¹
470 (Fig. 5C), and are combined differently to distinguish both genotypes. The 1332 and 1597 cm⁻¹
471 shifts are used twice in the classification trees, suggesting that both of these shifts are
472 important to differentiating the WT xylem fiber cell wall from the DM xylem fiber cell wall
473 (Fig. 5C). Interestingly, both bands are related to lignin compounds (1332 cm⁻¹: aliphatic O-H
474 bending; 1597 cm⁻¹: aromatic ring stretching) (Özparpucu *et al.*, 2017). The different
475 descriptors for the models built from the calibration and validation datasets range from 67 to
476 89%, suggesting that the models can be used to distinguish the xylem fiber cell wall
477 compositions of the two studied genotypes (Table 6).

478 To summarize, it seems that Raman shifts that discriminate cell walls between xylem
479 vessels of the two genotypes are related to polysaccharides while the cell walls between xylem
480 vessel/fibers and between adjacent fibers of the two genotypes can be discriminated using both
481 lignin and polysaccharides shifts. The application of a CART-based analysis enabled us to
482 identify new Raman shifts that could be used to better characterize the double mutant in a cell-
483 specific manner. Interestingly, our previous analysis of the *sweet11-1sweet12-1* double mutant
484 xylem cell wall did not reveal modifications in lignin composition (Le Hir *et al.*, 2015). These
485 discrepancies can be explained by the application of Raman microspectroscopy, which
486 provided a spatial resolution of 2 µm x 2 µm, and therefore, the possibility to investigate
487 individual cell types. The precision offered by Raman microspectroscopy suggests that the
488 differences observed between wild-type and the *sweet11-1sweet12-1* mutant line could depend
489 on the xylem cell type analyzed. Recently, Smith *et al.* (2017) demonstrated that xylem vessel
490 lignification in the *Arabidopsis* floral stem is a non-cell-autonomous process that relies on the
491 monolignol exchanges between xylem parenchyma or fiber cells and developing xylem vessels.
492 If this model is extended to our research, it could be suggested that in addition to monolignols,
493 sugar exchanges - mediated by SWEET facilitators - between xylem parenchyma cells and
494 developing xylem vessels could also be commonplace in *Arabidopsis*.

495

496

497 **Conclusion**

498 Synchrotron radiation FTIR and Raman spectroscopy are powerful tools for studying cell wall
499 composition in plants both at the tissue and cellular level. Here, the application of SR-FTIR
500 allowed us to picture the cell wall composition of phloem tissue in the *Arabidopsis* floral stem.
501 Furthermore, CART-based classification, calculated using the Raman spectra acquired for
502 different xylem cell types, identified spectral wavenumbers that could be leveraged to
503 discriminate xylem cell types based also on their cellulose and hemicellulose composition. We
504 also used both techniques to analyze the phenotype of the double mutant *sweet11-1sweet12-1*,
505 which is deficient in the expression of two sugar facilitators that exist in vascular parenchyma
506 cells. Our results showed changes in the hemicellulose composition of *sweet11-1sweet12-1*
507 phloem cell walls when compared to WT plants. Moreover, analysis by Raman spectroscopy
508 revealed that the disruption of both sugar transporters impacts xylem cell wall composition in
509 a cell-specific manner. Therefore, SWEET11 and SWEET12 are important to ensuring correct
510 phloem and xylem cell wall composition. Further addressing the role of SWEET facilitators in
511 plant growth and development provides an attractive research direction that could provide
512 answers for how intercellular sugar movements influence developmental processes such as
513 vascular system development. Additionally, this study highlights that vascular parenchyma
514 cells have a pivotal role in supplying the carbon skeleton required for cell wall formation in
515 vascular tissues. The research approach presented here offers therefore the possibility of
516 studying changes in cell wall polysaccharide composition at the cellular level and could be
517 applied to investigations of how sugar transport affects cell wall formation in the vascular tissue
518 of both herbaceous and ligneous species. Further, this approach open new perspectives for
519 studying mutants affected in lignin biosynthesis and structure in the different xylem cell types,
520 including, for instance, comparison between xylary fibers and interfascicular fibers.

521

522 **Supplementary data**

523 **Fig. S1.** Illustration of the different spatial resolutions offered by vibrational spectroscopy
524 techniques.

525 **Fig. S2.** Comparison of SR-FTIR peak areas of cellulose, hemicelluloses and lignin between
526 xylem or phloem tissues from WT and *sweet11-1sweet12-1* plants.

527 **Fig. S3.** Average Raman spectra for the different xylem cell types in wild-type and *sweet11-*
528 *1sweet12-1* lines.

529

530 **Acknowledgements**

531 We thank Bruno Letarne for his assistance in the greenhouse. The research was supported by
532 the SOLEIL, the French national synchrotron facility (project n° 20150210). This work
533 benefitted from a French State grant (LabEx Saclay Plant Sciences-SPS, ref. ANR-10-LABX-
534 0040-SPS), managed by the French National Research Agency under an "Investments for the
535 Future" program (ref. ANR-11-IDEX-0003-02). The authors declare no competing financial
536 interests. The ChemFlow interface was supported by the Agropolis Foundation under the
537 reference ID-1401-005 through the "Investissements d'Avenir" program (Labex Agro: ANR-
538 10-LABX-0001-01).

539

References

Agarwal UP. 2006. Raman imaging to investigate ultrastructure and composition of plant cell walls: Distribution of lignin and cellulose in black spruce wood (*Picea mariana*). *Planta* **224**, 1141–1153.

Agarwal UP. 2014. 1064 nm FT-Raman spectroscopy for investigations of plant cell walls and other biomass materials. *Frontiers in plant science* **5**, 1–12.

Bekiaris G, Lindedam J, Peltre C, Decker SR, Turner GB, Magid J, Bruun S. 2015. Rapid estimation of sugar release from winter wheat straw during bioethanol production using FTIR-photoacoustic spectroscopy. *Biotechnology for Biofuels* **8**, 1–12.

Beleites C. 2012. Package ‘hyperSpec’. CRAN package.

Berk RA. 2016. Classification and Regression Trees (CART). Statistical learning from a regression perspective. Cham, Switzerland: Springer Nature, 103–167.

Brown DM, Zeef LAH, Ellis J, Goodacre R, Turner SR. 2005. Identification of novel genes in *Arabidopsis* involved in secondary cell wall formation using expression profiling and reverse genetics. *The Plant Cell* **17**, 2281–2295.

Brown DM, Zhang Z, Stephens E, Dupree P, Turner SR. 2009. Characterization of IRX10 and IRX10-like reveals an essential role in glucuronoxylan biosynthesis in *Arabidopsis*. *Plant Journal* **57**, 732–746.

Chen L-Q, Qu X-Q, Hou B-H, Sosso D, Osorio S, Fernie AR, Frommer WB. 2012. Sucrose efflux mediated by SWEET proteins as a key step for phloem transport. *Science* **335**, 207–211.

Chylinska M, Szymanska-Charget M, Zdunek A. 2014. Imaging of polysaccharides in the tomato cell wall with Raman microspectroscopy. *Plant methods* **10**, 1–9.

Devaux M-F, Jamme F, André W, Bouchet B, Alvarado C, Durand S, Robert P, Saulnier L, Bonnin E, Guillot F. 2018. Synchrotron time-lapse imaging of lignocellulosic biomass hydrolysis: tracking enzyme localization by protein autofluorescence and biochemical modification of cell walls by microfluidic infrared microspectroscopy. *Frontiers in Plant Science* **9**, 1–16.

Earley EJ, Ingland B, Winkler J, Tonsor SJ. 2009. Inflorescences contribute more than rosettes to lifetime carbon gain in *Arabidopsis thaliana* (Brassicaceae). *American Journal of*

Botany **96**, 786–792.

Edwards HG, Farwell DW, Webster D. 1997. FT Raman microscopy of untreated natural plant fibres. *Spectrochimica Acta. Part A, Molecular and Biomolecular Spectroscopy* **53**, 2383–2392.

Esau K, Cheadle VI. 1958. Wall Thickening in Sieve Elements. *Proceedings of the National Academy of Sciences of the USA* **44**, 546–553.

Faix O. 1991. Classification of lignins from different botanical origins by FT-IR spectroscopy. *Holzforschung-International Journal of the Biology, Chemistry, Physics and Technology of Wood* **45**, 21–28.

Freshour G, Clay RP, Fuller MS, Albersheim P, Darvill AG, Hahn MG. 1996. Developmental and tissue-specific structural alterations of the cell-wall polysaccharides of *Arabidopsis thaliana* roots. *Plant Physiology* **110**, 1413–1429.

Gierlinger N. 2017. New insights into plant cell walls by vibrational microspectroscopy. *Applied Spectroscopy Reviews* **49**, 28, 1–35.

Gierlinger N, Keplinger T, Harrington M. 2012. Imaging of plant cell walls by confocal Raman microscopy. *Nature Protocols* **7**, 1694–1708.

Gierlinger N, Sapei L, Paris O. 2008. Insights into the chemical composition of *Equisetum hyemale* by high resolution Raman imaging. *Planta* **227**, 969–980.

Gierlinger N, Schwanninger M. 2007. The potential of Raman microscopy and Raman imaging in plant research. *Spectroscopy* **21**, 69–89.

Gorzsás A, Stenlund H, Persson P, Trygg J, Sundberg B. 2011. Cell-specific chemotyping and multivariate imaging by combined FT-IR microspectroscopy and orthogonal projections to latent structures (OPLS) analysis reveals the chemical landscape of secondary xylem. *Plant Journal* **66**, 903–914.

Guillon F, Bouchet B, Jamme F, Robert P, Quéméner B, Barron C, Larré C, Dumas P, Saulnier L. 2011. *Brachypodium distachyon* grain: characterization of endosperm cell walls. *Journal of Experimental Botany* **62**, 1001–1015.

Hall HC, Cheung J, Ellis BE. 2013. Immunoprofiling reveals unique cell-specific patterns of wall epitopes in the expanding *Arabidopsis* stem. *Plant Journal* **74**, 134–147.

Hänninen T, Kontturi E, Vuorinen T. 2011. Distribution of lignin and its coniferyl alcohol and coniferyl aldehyde groups in *Picea abies* and *Pinus sylvestris* as observed by Raman imaging. *Phytochemistry* **72**, 1889–1895.

Le Hir R, Beneteau J, Bellini C, Vilaine F, Dinant S. 2008. Gene expression profiling: keys for investigating phloem functions. *Trends in Plant Science* **13**, 273–280.

Le Hir R, Spinner L, Klemens PAW, et al. 2015. Disruption of the Sugar Transporters AtSWEET11 and AtSWEET12 Affects Vascular Development and Freezing Tolerance in *Arabidopsis*. *Molecular Plant* **8**, 1687–1990.

Horbens M, Feldner A, Höfer M, Neinhuis C. 2014. Ontogenetic tissue modification in *Malus* fruit peduncles: The role of sclereids. *Annals of Botany* **113**, 105–118.

Hothorn T, Hornik K, Wiel MA van de, Zeileis A. 2008. Implementing a Class of Permutation Tests: the coin Package. *Journal of Statistical Software* **28**, 1–23.

Jin K, Liu X, Wang K, Jiang Z, Tian G, Yang S, Shang L, Ma J. 2018. Imaging the dynamic deposition of cell wall polymer in xylem and phloem in *Populus × euramericana*. *Planta*, 1–10.

Johnson K. 2018. Sugar coating the phloem sieve element wall. *Plant Physiology* **176**, 1408–1409.

Kačuráková M, Smith AC, Gidley MJ, Wilson RH. 2002. Molecular interactions in bacterial cellulose composites studied by 1D FT-IR and dynamic 2D FT-IR spectroscopy. *Carbohydrate Research* **337**, 1145–1153.

Kim JS, Daniel G. 2012. Immunolocalization of hemicelluloses in *Arabidopsis thaliana* stem. Part I: Temporal and spatial distribution of xylans. *Planta* **236**, 1275–1288.

Kubo S, Kadla JF. 2005. Hydrogen bonding in lignin: a fourier transform infrared model compound study. *Biomacromolecules* **6**, 2815–2821.

Largo-Gosens A, Hernández-Altamirano M, Garcí-a-Calvo L, Alonso-Simón A, Álvarez J, Acebes J. 2014. Fourier transform mid infrared spectroscopy applications for monitoring the structural plasticity of plant cell walls. *Frontiers in Plant Science* **5**, 1–15.

Lefebvre V, Fortabat M-N, Ducamp A, North HM, Maia-Grondard A, Trouverie J, Boursiac Y, Mouille G, Durand-Tardif M. 2011. ESKIMO1 disruption in *Arabidopsis* alters vascular tissue and impairs water transport. *PLoS One* **6**, e16645.

Marchessault R. 1962. Application of infra-red spectroscopy to cellulose and wood polysaccharides. *Pure Applied Chemistry* **5**, 107–129.

Marchessault R, Liang C. 1962. The infrared spectra of crystalline polysaccharides VIII. Xylans. *Journal of polymer science part A-Polymer Chemistry* **59**, 357–378.

Marriott PE, Gómez LD, Mcqueen-Mason SJ. 2016. Unlocking the potential of lignocellulosic biomass through plant science. *New Phytologist* **209**, 1366–1381.

Maru V, Hewale S, Mantri H, Ranade V. 2015. Partial purification and characterization of mannan oligosaccharides from cell wall of *Saccharomyces cerevisiae*. *International Journal of Current Microbiology and Applied Sciences* **4**, 705–711.

Maxime H. 2017. RVAideMemoire: diverse basic statistical and graphical functions. R package 0.9-57.

De Meester B, De Vries L, Özparpucu M, et al. 2017. Vessel-specific reintroduction of CINNAMOYL COA REDUCTASE 1 (CCR1) in dwarfed ccr1 mutants restores vessel and xylary fiber integrity and increases biomass. *Plant Physiology* **176**, 611–633.

Mohebby B. 2010. Application of ATR infrared spectroscopy in wood acetylation. *Journal of Agricultural Science and Technology* **10**, 253–259.

Mouille G, Robin S, Lecomte M, Pagant S, Hofte H. 2003. Classification and identification of *Arabidopsis* cell wall mutants using Fourier-Transform InfraRed (FT-IR) microspectroscopy. *Plant Journal* **35**, 393–404.

Mouille G, Witucka-Wall H, Bruyant MP, Loudet O, Pelletier S, Rihouey C, Lerouxel O, Lerouge P, Höfte H, Pauly M. 2006. Quantitative trait loci analysis of primary cell wall composition in *Arabidopsis*. *Plant Physiology* **141**, 1035–1044.

Ohman D, Demedts B, Kumar M, Gerber L, Gorzsás A, Goeminne G, Hedenström M, Ellis B, Boerjan W, Sundberg B. 2013. MYB103 is required for FERULATE-5-HYDROXYLASE expression and syringyl lignin biosynthesis in *Arabidopsis* stems. *Plant Journal* **73**, 63–76.

Owen NL, Thomas DW. 1989. Infrared studies of ‘hard’ and ‘soft’ woods. *Applied Spectroscopy* **43**, 451–455.

Özparpucu M, Gierlinger N, Burgert I, Van Acker R, Vanholme R, Boerjan W, Pilate G,

Déjardin A, Rüggeberg M. 2018. The effect of altered lignin composition on mechanical properties of CINNAMYL ALCOHOL DEHYDROGENASE (CAD) deficient poplars. *Planta* **247**, 887–897.

Özparpucu M, Rüggeberg M, Gierlinger N, Cesarino I, Vanholme R, Boerjan W, Burgert I. 2017. Unravelling the impact of lignin on cell wall mechanics: a comprehensive study on young poplar trees downregulated for CINNAMYL ALCOHOL DEHYDROGENASE (CAD). *Plant Journal* **91**, 480–490.

Pawar PM-A, Koutaniemi S, Tenkanen M, Mellerowicz EJ. 2013. Acetylation of woody lignocellulose: significance and regulation. *Frontiers in Plant Science* **4**, 1–8.

Pelloux J, Rusterucci C, Mellerowicz EJ. 2007. New insights into pectin methylesterase structure and function. *Trends in Plant Science* **12**, 267–277.

Pereira L, Flores-Borges D, Bittencourt P, Mayer J, Kiyota E, Araújo P, Jansen S, Freitas R, Oliveira R, Mazzafera P. 2018. Infrared nanospectroscopy reveals the chemical nature of pit membranes in water-conducting cells of the plant xylem. *Plant Physiology* **166**, pp.00138.2018.

Persson S, Caffall KH, Freshour G, Hille MT, Bauer S, Poindexter P, Hahn MG, Mohnen D, Somerville C. 2007. The *Arabidopsis* irregular xylem8 mutant is deficient in glucuronoxylan and homogalacturonan, which are essential for secondary cell wall integrity. *The Plant Cell Online* **19**, 237–255.

Prats Mateu B, Hauser MT, Heredia A, Gierlinger N. 2016. Waterproofing in *Arabidopsis*: Following Phenolics and Lipids In situ by Confocal Raman Microscopy. *Frontiers in chemistry* **4**, 1–13.

R Development Core Team. 2016. R: a language and environment for statistical computing. [2.12.2]. R Foundation for Statistical Computing, Vienna, Austria. URL <http://www.R-project.org/>.

Robin S, Lecomte M, Höfte H, Mouille G. 2003. A procedure for the clustering of cell wall mutants in the model plant *Arabidopsis* based on Fourier-transform infrared (FT-IR) spectroscopy. *Journal of Applied Statistics* **30**, 669–681.

Roger JM, Palagos B, Bertrand D, Fernandez-Ahumada E. 2011. CovSel: Variable selection for highly multivariate and multi-response calibration. Application to IR

spectroscopy. *Chemometrics and Intelligent Laboratory Systems* **2**, 216–223.

Schmidt M, Schwartzberg AM, Carroll A, Chaibang A, Adams PD, Schuck PJ. 2010. Raman imaging of cell wall polymers in *Arabidopsis thaliana*. *Biochemical and Biophysical Research Communications* **395**, 521–523.

Schuetz M, Smith R, Ellis B. 2012. Xylem tissue specification, patterning, and differentiation mechanisms. *Journal of Experimental Botany* **64**, 11–31.

Sibout R, Eudes A, Mouille G, Pollet B, Lapierre C, Jouanin L, Séguin A. 2005. CINNAMYL ALCOHOL DEHYDROGENASE-C and -D are the primary genes involved in lignin biosynthesis in the floral stem of *Arabidopsis*. *The Plant cell* **17**, 2059–2076.

Sjölund RD. 1997. The phloem sieve elements: a river runs through it. *Plant Cell* **9**, 1137–1146.

Smith RA, Schuetz M, Karlen SD, Bird D, Tokunaga N, Sato Y, Mansfield SD, Ralph J, Samuels AL. 2017. Defining the Diverse Cell Populations Contributing to Lignification in *Arabidopsis thaliana* Stems. *Plant Physiology* **174**, 1028–1036.

Strabala TJ, MacMillan CP. 2013. The *Arabidopsis* wood model—the case for the inflorescence stem. *Plant Science* **210**, 193–205.

Tolbert AK, Ma T, Kalluri UC, Ragauskas AJ. 2016. Determining the syringyl/guaiacyl lignin ratio in the vessel and fiber cell walls of transgenic *Populus* plants. *Energy and Fuels* **30**, 5716–5720.

Torode TA, O'Neill RE, Marcus SE, et al. 2018. Branched pectic galactan in phloem-sieve-element cell walls: implications for cell mechanics. *Plant Physiology* **176**, 1547–1558.

Vijayan P, Willick IR, Lahlali R, Karunakaran C, Tanino KK. 2015. Synchrotron radiation sheds fresh light on plant research: The use of powerful techniques to probe structure and composition of plants. *Plant and Cell Physiology* **56**, 1252–1263.

Wickham H. 2009. *ggplot2 elegant graphics for data analysis*. Cham, Switzerland: Springer Nature.

Zeise I, Heiner Z, Holz S, Joester M, Büttner C, Kneipp J. 2018. Raman imaging of plant cell walls in sections of *Cucumis sativus*. *Plants* **7**, 1–16.

Zhang M, Lapierre C, Nouxman NL, Nieuwoudt MK, Smith BG, Chavan RR, McArdle

BH, Harris PJ. 2017. Location and characterization of lignin in tracheid cell walls of radiata pine (*Pinus radiata* D. Don) compression woods. *Plant Physiology and Biochemistry* **118**, 187–198.

Zhang C, Turgeon R. 2018. Mechanisms of phloem loading. *Current Opinion in Plant Biology* **43**, 71–75.

Zimmermann B, Bağcioletlu M, Sandt C, Kohler A. 2015. Vibrational microspectroscopy enables chemical characterization of single pollen grains as well as comparative analysis of plant species based on pollen ultrastructure. *Planta* **242**, 1237–1250.

Table 1. Assignment of the infrared wavenumbers found to differentiate xylem and phloem tissues of the wild-type *Arabidopsis* floral stem.

Tissue	FTIR wavenumber (cm ⁻¹)	Assignment	Polymer
Xylem	1510	G-type lignin (Faix, 1991)	Lignin
	1595	G-type lignin (Faix, 1991)	Lignin
	1269	Guaiacyl ring breathing with carbonyl stretching (Kubo and Kadla, 2005)	Lignin
	1030	C-H deformation in guaiacyl with C-O deformation in the primary alcohol (Kubo and Kadla, 2005)	Lignin
	1060	C-C linkage of G condensed unit (Sibout <i>et al.</i> , 2005)	Lignin
	1045	C-O-C contribution of xylan (Brown <i>et al.</i> , 2009)	Hemicellulose
	1369	Deformation of the C-H linkages in the methyl group of <i>O</i> -acetyl moieties (Mohebby, 2010)	Hemicellulose
	1230-1235	C=O/C-O linkages stretching vibrations (Mohebby, 2010)	Hemicellulose
	1743	Stretching of the free carbonyl group (Owen and Thomas, 1989)	Hemicellulose
	1245	C-O stretch (Faix, 1991)	Hemicellulose
	1735-1740	C=O stretching in glucuronic acid (xylan) (Marchessault, 1962; Marchessault and Liang, 1962)	Hemicellulose
	1762	Esterified pectins (Kačuráková <i>et al.</i> , 2002)	Pectins
Phloem	1639	COOH group (Mouille <i>et al.</i> , 2006)	Acidic pectins
	1677	COOH group (Mouille <i>et al.</i> , 2006)	Acidic pectins
	1157	C-O-C linkages of cellulose (Kačuráková <i>et al.</i> , 2002)	Cellulose
	1442	To be assigned (Mouille <i>et al.</i> , 2003)	Related to primary cell wall
	1111	In plane ring stretching (Bekiaris <i>et al.</i> , 2015)	Cellulose
	1712	C=O stretch (Kačuráková <i>et al.</i> , 2002)	Pectins
	978	Xylan-type polysaccharides (Brown <i>et al.</i> , 2005)	Hemicellulose
	958	Sugar ring vibrations (Kačuráková <i>et al.</i> , 2002)	Pectins
	1475	To be assigned	To be assigned
	1550	Carboxylates (Mouille <i>et al.</i> , 2006)	Cellulose
	1774	To be assigned	Esterified pectins

Table 2. Classification results for using FTIR wavenumbers to predict which genotype a phloem tissue sample represents, with the model calibration dataset (80% of total dataset) using a ten-fold cross-validation method, and the validation dataset (20% of total dataset) using a CART-based algorithm. NPV: negative predictive value, PPV: positive predictive value.

Calibration model (after ten-fold cross-validation)		Prediction		Accuracy 90.5%
		wild-type	<i>sweet11sweet12</i>	
	wild-type	125	10	PPV 92.6%
	<i>sweet11sweet12</i>	16	124	NPV 88.6%
		Sensitivity 88.6%	Specificity 92.5%	
Validation model		Prediction		Accuracy 80.9%
		wild-type	<i>sweet11sweet12</i>	
	wild-type	24	8	PPV 75%
	<i>sweet11sweet12</i>	5	31	NPV 86.1%
		Sensitivity 82.7%	Specificity 79.5%	

Table 3. Classification results for using Raman shifts to predict different xylem cell types, with the model calibration dataset (80% of the total dataset) using a ten-fold cross-validation method, and the validation dataset (20% of the total dataset) using a CART-based algorithm. For the calculation of the different parameters, one cell type was compared to the two others. FF: cell wall between two xylem fibers, NPV: negative predictive value, PPV: positive predictive value, VF: cell wall between xylem vessel and fiber, VV: cell wall between two xylem vessels.

		Raman prediction			Accuracy 85.9%
		VV	VF	FF	
Calibration model (after ten-fold cross- validation)	VV	18	0	0	PPV/NPV 100%/86.9%
	VF	6	27	1	PPV/NPV 77.7%/90%
	FF	0	2	10	PPV/NPV 83.3%/98%
		Sensitivity/Specificity 0.75/0.869	Sensitivity/Specificity 0.931/0.72	Sensitivity/Specificity 0.90/0.962	
Validation model		Raman prediction			Accuracy 80%
		VV	VF	FF	
		4	4	0	PPV/NPV 50%/84.6%
		0	14	2	PPV/NPV 87.5%/71.4%
		0	0	6	PPV/NPV 100%/91.6%
		Sensitivity/Specificity 100%/84.6%	Sensitivity/Specificity 77.7%/83.3%	Sensitivity/Specificity 75%/100%	

Table 4. Classification results for using Raman shifts to predict which genotype cell walls between xylem vessels represent, with the model calibration dataset (80% of total dataset) using a ten-fold cross-validation method, and the validation dataset (20% of total dataset) using a CART-based algorithm. NPV: negative predictive value, PPV: positive predictive value.

Xylem vessel /Xylem vessel			Raman prediction		Accuracy 88.9%
			wild-type	<i>sweet11sweet12</i>	
	Calibration model (after ten-fold cross- validation)	wild-type	33	2	PPV 94.3%
		<i>sweet11sweet12</i>	7	39	NPV 84.8%
			Sensitivity 82.5%	Specificity 95.1%	
			Raman prediction		Accuracy 84.2%
	Validation model	wild-type	10	1	PPV 90.9%
		<i>sweet11sweet12</i>	2	6	NPV 75%
			Sensitivity 83.3%	Specificity 85.7%	

Table 5. Classification results for using Raman shifts to predict which genotype cell walls between a xylem vessel and fiber represent, with the model calibration dataset (80% of total dataset) using a ten-fold cross-validation method, and the validation dataset (20% of total dataset) using a CART-based algorithm. NPV: negative predictive value, PPV: positive predictive value.

		Raman prediction		Accuracy 84.8%	
		wild-type	<i>sweet11sweet12</i>		
Xylem vessel /Xylem fiber	Calibration model (after ten-fold cross- validation)	wild-type	82	12	PPV 87.2%
		<i>sweet11sweet12</i>	30	152	NPV 83.5%
			Sensitivity 73.2%	Specificity 92.7%	
	Validation model	Raman prediction		Accuracy 88.4%	
		wild-type	<i>sweet11sweet12</i>		
		wild-type	17	6	PPV 73.9%
		<i>sweet11sweet12</i>	2	44	NPV 95.6%
			Sensitivity 89.5%	Specificity 88%	

Table 6. Classification results for using Raman shifts to predict which genotype cell walls between xylem fibers represent, with the model calibration dataset (80% of total dataset) using a ten-fold cross-validation method, and the validation dataset (20% of total dataset) using a CART-based algorithm. NPV: negative predictive value, PPV: positive predictive value.

Xylem fiber /Xylem fiber			Raman prediction		Accuracy 83.8%
			wild-type	<i>sweet11sweet12</i>	
	Calibration model (after ten-fold cross- validation)	wild-type	90	14	PPV 86.5%
		<i>sweet11sweet12</i>	11	39	NPV 78%
			Sensitivity 89.1%	Specificity 73.6%	
			Raman prediction		Accuracy 73.7%
	Validation model	wild-type	14	3	PPV 82.3%
		<i>sweet11sweet12</i>	7	14	NPV 66.7%
			Sensitivity 66.7%	Specificity 82.3%	

Figure Legends

Fig. 1. Workflow for the floral stem vascular system analysis by SR-FTIR and Raman spectroscopy.

Schematic representation of a floral stem vascular bundle showing the phloem (light gray) and the xylem (dark gray) and the size of the acquisition zone for SR-FTIR and Raman analysis. SR-FTIR was used to obtain tissue-specific signature by PCA analysis of the spectra acquired on phloem and xylem cell walls of the WT plants. Additionally, a genetic effect was assessed by SR-FTIR by analyzing spectra of WT and mutant line with spectral peak areas ratios and CART-based classification. Then Raman microspectroscopy was used to obtain cell-specific interfaces signature on the different xylem cell types and to assess the genetic effect in a mutant line by spectral peak areas ratios and CART-based classification. F: fiber; Ph: phloem; SR-FTIR: synchrotron radiation fourier-transformed infrared spectroscopy; V: vessel; Xy: xylem.

Fig. 2. Principal Component Analysis (PCA) of infrared spectra obtained from phloem and xylem cells of *Arabidopsis* wild-type floral stem.

(A) Average spectra for wild-type phloem (red line) and xylem (blue line) tissues obtained by SR-FTIR microscopy. Spectra were baseline-corrected and area-normalized in the range of 1800-850 cm⁻¹. (B) Comparison of phloem and xylem cell wall composition by multivariate analysis. Spectra from xylem (blue boxes) or phloem (red circles) cell walls were compared. A scoreplot based on PC1 and PC2 from the Principal Component Analysis (PCA) shows that phloem and xylem cell wall spectral signatures can be differentiated. (C) The corresponding loading plot of the PC1 axis is presented.

Fig. 3. Comparative analysis of wild-type and *sweet11-1sweet12-1* xylem or phloem SR-FTIR spectra.

(A-B) Boxplot representation of the hemicellulose/cellulose ratio of xylem (A) and phloem (B) spectra. For the xylem spectra, the box and whisker plots represent values from 521 and 494 individual spectra of wild-type and *sweet11-1sweet12-1* lines, respectively. For the phloem spectra, the box and whisker plots represent the values from 314 and 311 individual spectra of wild-type and *sweet11-1sweet12-1* lines, respectively. The diamonds represent mean values, lines represent median values, the tops and bottoms of the boxes represent the first and third

quartiles, respectively, and whisker extremities represent maximum and minimum data points. The black dots are the outliers. Letters above the boxes indicate groups with significant differences as determined by an approximate Fisher-Pitman permutation test and a pairwise comparison test ($P < 0.05$). a.u.: arbitrary unit. (C) The classification tree has been generated by the CART method after ten-fold cross-validation of the calibration dataset model, which was built using the 850-1800 cm^{-1} range of phloem spectra. The binary classification tree is composed of five classifiers and 6 terminal subgroups. The decision-making process involves the evaluation of if-then rules of each node from top to bottom, which eventually reaches a terminal node with the designated class outcome (WT: wild-type and DM: *sweet11-1sweet12-1*). The numbers in each terminal subgroup represent numbers of either WT or DM spectra.

Fig. 4. Raman spectra analysis of the different xylem cell types in wild-type plants.

(A-C) Boxplot representation of the lignin/C-H stretching band ratio (A), lignin/C-O and C-C bond stretching ratio (B) and C-H stretching band/C-O and C-C bond stretching ratio (C) in secondary cell walls between different xylem cell types. The box and whisker plots represent values from 51, 139 and 119 individual spectra of VV, VF and FF, respectively. The diamonds represent mean values, lines represent median values, the tops and bottoms of the boxes represent the first and third quartiles, respectively, and whisker extremities represent maximum and minimum data points. The black dots are the outliers. Letters above the boxes indicate groups with significant differences as determined by an approximate Fisher-Pitman permutation test and a pairwise comparison test ($P < 0.05$). a.u.: arbitrary unit. (F) The classification tree has been generated by the CART method after ten-fold cross-validation of the calibration dataset model, which was built using the 1000-1800 cm^{-1} range from the Raman spectra of different xylem cell types. The binary classification tree is composed of four classifiers and 5 terminal subgroups. The decision-making process involves the evaluation of if-then rules of each node from top to bottom, which eventually reaches a terminal node with the designated class outcome (VV: vessel/vessel cell wall, VF: vessel/fiber cell wall and FF: fiber/fiber cell wall). The numbers in each terminal subgroup stand for the number of VV, VF or FF spectra.

Fig. 5. CART classification of wild-type and *sweet11-1sweet12-1* xylem Raman spectra.

The classification trees have been generated by the CART method after ten-fold cross-

validation of the calibration dataset model, which was built using the 1800-1000 cm^{-1} range from the Raman spectra of cell walls between two xylem vessels (A), between a xylem vessel and a fiber (B) and between two xylem fibers (C). The decision-making process involves the evaluation of if-then rules of each node from top to bottom, which eventually reaches a terminal node with the designated class outcome (WT: wild-type and DM: *sweet11-1sweet12-1*). The numbers in each terminal subgroup stand for the number of either WT or DM spectra.

Fig. 1

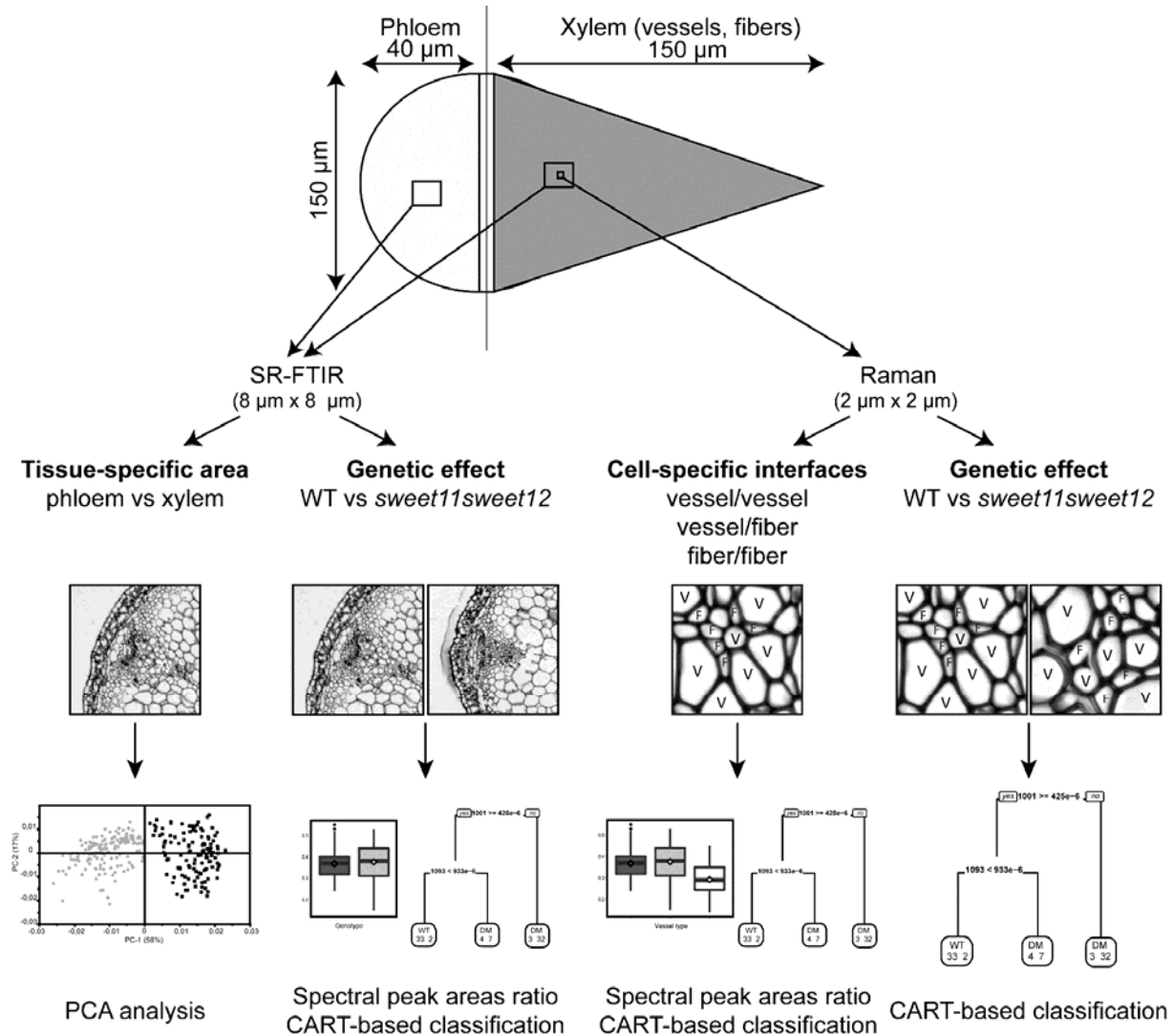


Fig. 2

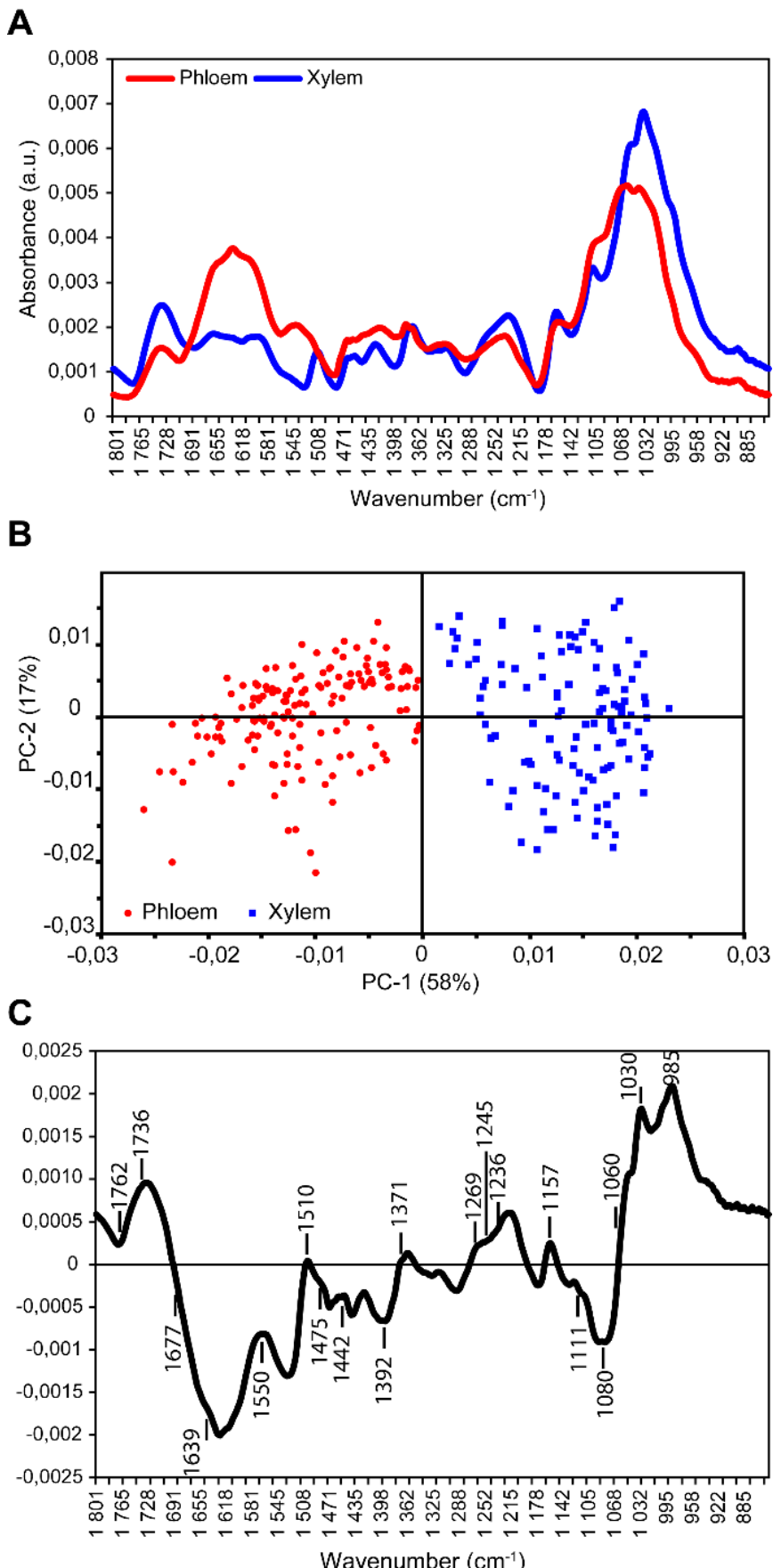


Fig. 3

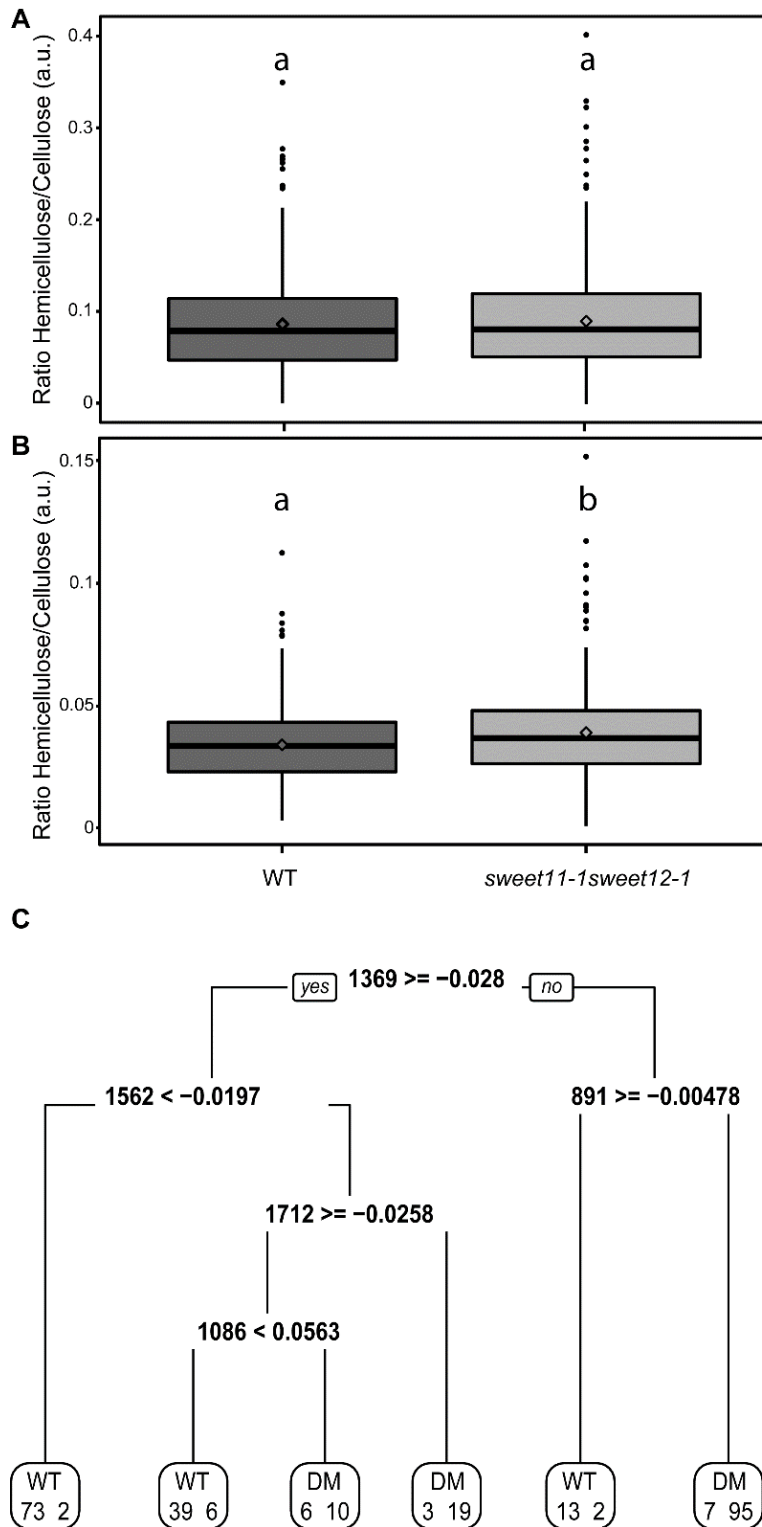


Fig. 4

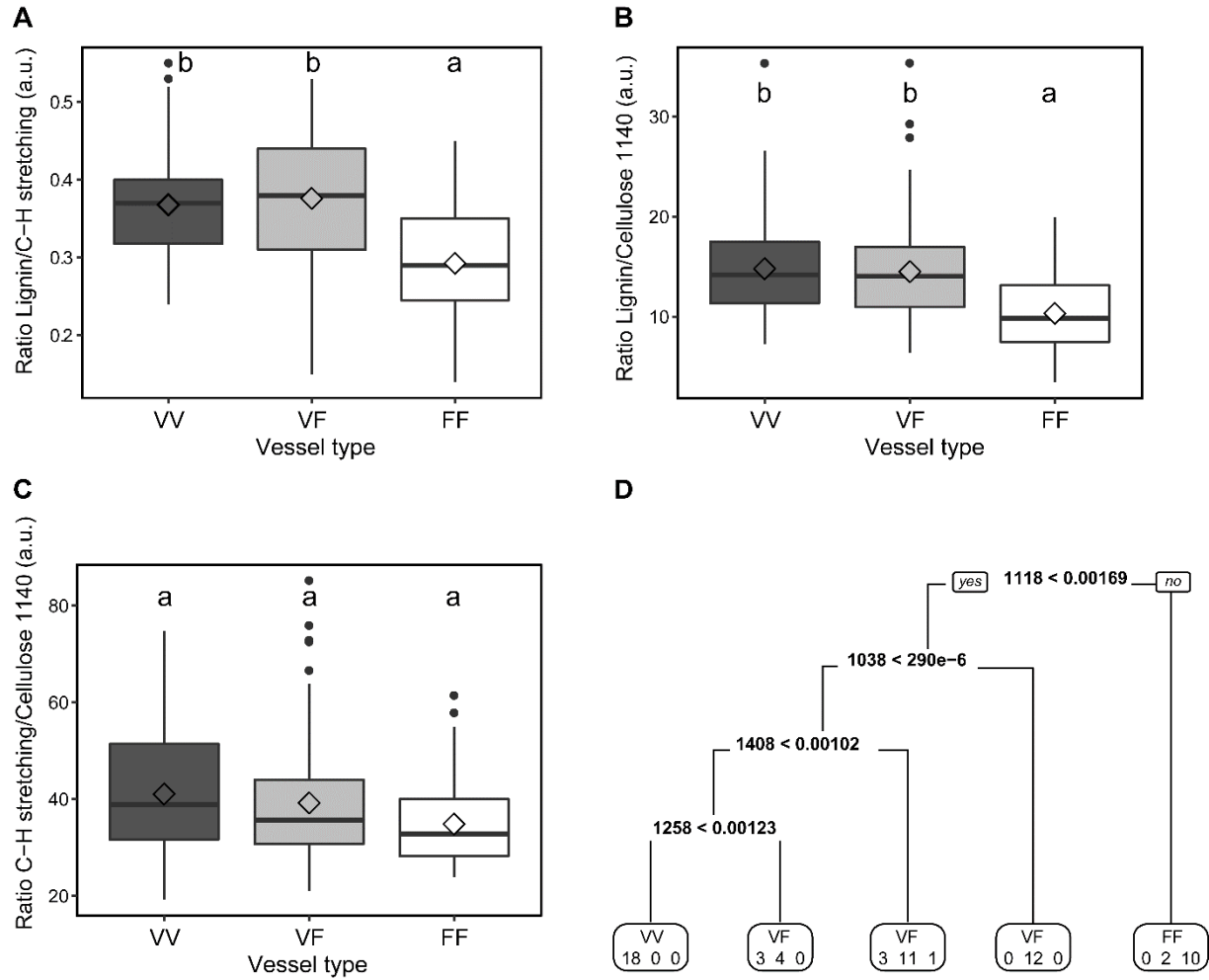


Fig. 5

